

Continental configuration controls ocean oxygenation during the Phanerozoic

<https://doi.org/10.1038/s41586-022-05018-z>

Received: 17 September 2021

Accepted: 23 June 2022

Published online: 17 August 2022

 Check for updates

Alexandre Pohl^{1,2,8}✉, Andy Ridgwell^{1,8}, Richard G. Stockey³, Christophe Thomazo^{2,4}, Andrew Keane^{5,6}, Emmanuelle Vennin² & Christopher R. Scotese⁷

The early evolutionary and much of the extinction history of marine animals is thought to be driven by changes in dissolved oxygen concentrations ($[O_2]$) in the ocean^{1–3}. In turn, $[O_2]$ is widely assumed to be dominated by the geological history of atmospheric oxygen (pO_2)^{4,5}. Here, by contrast, we show by means of a series of Earth system model experiments how continental rearrangement during the Phanerozoic Eon drives profound variations in ocean oxygenation and induces a fundamental decoupling in time between upper-ocean and benthic $[O_2]$. We further identify the presence of state transitions in the global ocean circulation, which lead to extensive deep-ocean anoxia developing in the early Phanerozoic even under modern pO_2 . Our finding that ocean oxygenation oscillates over stable thousand-year (kyr) periods also provides a causal mechanism that might explain elevated rates of metazoan radiation and extinction during the early Palaeozoic Era⁶. The absence, in our modelling, of any simple correlation between global climate and ocean ventilation, and the occurrence of profound variations in ocean oxygenation independent of atmospheric pO_2 , presents a challenge to the interpretation of marine redox proxies, but also points to a hitherto unrecognized role for continental configuration in the evolution of the biosphere.

The availability of dissolved oxygen in the ocean exerts a critical control on habitability for marine animals^{1,7} and is thought to have strongly affected their evolution from the late Neoproterozoic and through the Phanerozoic Eon (541–0 million years ago (Ma))^{1–3}. Indeed, the emergence of the first unambiguous metazoans during the Ediacaran Period (635–541 Ma) may have been triggered by the occurrence of ambient dissolved oxygen concentrations ($[O_2]$) sufficient to support the metabolism of a large body size¹. Further increases in ocean oxygenation may have contributed to the Great Ordovician Biodiversification Event⁸ as well as the rise of large predatory fish in the Devonian⁹. Conversely, episodic deoxygenation is considered the primary kill mechanism during many of the main Phanerozoic mass extinction events, including the Late Ordovician¹⁰, Late Devonian¹¹ and end Permian⁷.

The past few decades have seen the development and application of a variety of geochemical redox proxies, such as $\delta^{238}\text{U}$ (ref. ¹²), $\delta^{98}\text{Mo}$ (ref. ⁹), I/Ca (ref. ¹³) and iron speciation¹⁴, which have provided us with unprecedented insights into the Phanerozoic history of ocean oxygenation^{5,13}. In parallel, numerical models have been instrumental in helping interpret the proxy trends and test hypotheses for the underlying driving mechanisms^{4,15}. Principal among the ideas that have arisen is that changes in atmospheric pO_2 can be inferred from the ocean^{4,5,15}. However, for computational reasons, this link between ocean $[O_2]$ and atmospheric pO_2 has invariably been made without considering how ocean circulation may have changed over time^{4,5,15}. Although the

importance of continental configuration for ocean circulation and surface climate has started to be studied systematically^{16–18}, spatial patterns of ocean geochemistry and redox have only been considered in a limited number of continental configurations (such as refs. ^{7,19}) and often analysed in temporal isolation. Here we explicitly address this gap using an Earth system model of intermediate complexity to quantify how continental configuration can modulate the distribution of $[O_2]$ in the ocean, thereby leading us to a radically different conclusion about the inferences that can be drawn from marine redox proxy records.

We base our analysis on a series of past ocean circulation scenarios generated using cGENIE²⁰, an Earth system model of intermediate complexity designed to simulate the large-scale biogeochemical cycles and patterns in the ocean, and one that has previously been shown to be capable of simulating regional-scale distributions of $[O_2]$ in the present-day ocean²⁰ as well as in the geological past^{19,21} (see Methods and Extended Data Fig. 1). In these experiments, we consider both the potential role of changing ecological structure in the ocean (using the size-structured plankton model of ref. ²²) as well as the influence of temperature on metabolic rates (following ref. ²³) in creating 3D realizations of the potential distribution of $[O_2]$ in the ocean. On the basis of the continental reconstructions of Scotese and Wright²⁴, we conducted one simulation every 20 Myr through the Phanerozoic, for a total of 28 simulated time slices. To help isolate the impact of continental configuration from other changes occurring through the Phanerozoic, only the continental configuration²⁴ (plus physical atmospheric boundary

¹Department of Earth and Planetary Sciences, University of California, Riverside, Riverside, CA, USA. ²Biogéosciences, UMR 6282, UBFC/CNRS, Université Bourgogne Franche-Comté, Dijon, France. ³Department of Geological Sciences, Stanford University, Stanford, CA, USA. ⁴Institut Universitaire de France, Paris, France. ⁵School of Mathematical Sciences, University College Cork, Cork, Ireland. ⁶Environmental Research Institute, University College Cork, Cork, Ireland. ⁷Department of Earth and Planetary Sciences, Northwestern University, Evanston, IL, USA. ⁸These authors contributed equally: Alexandre Pohl, Andy Ridgwell. [✉]e-mail: alexandre.pohl@u-bourgogne.fr

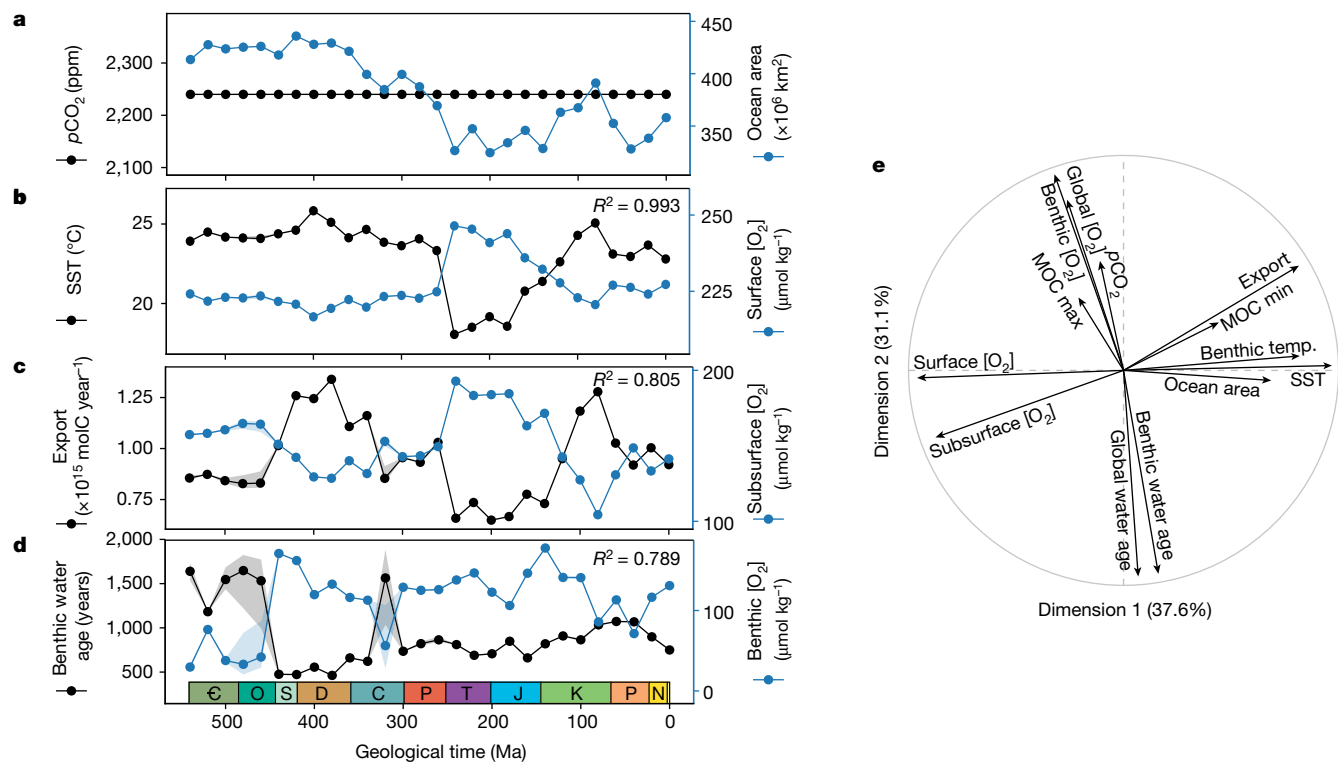


Fig. 1 | Earth system model results for simulations at 2,240 ppm CO_2 (series #1). **a**, Atmospheric $p\text{CO}_2$ and global ocean area. **b**, Globally averaged SSTs and globally averaged ocean-surface oxygen concentrations. **c**, Total export production and globally averaged subsurface (around 90–190 m depth) oxygen concentrations. **d**, Globally averaged benthic water age and benthic oxygen concentrations, both extracted below 1,000 m depth. **e**, Principal

component analysis (Methods). In panels **b–d**, the linear correlation coefficient (R^2) value is provided in the upper-right corner. For each variable and age, the mean value simulated over the last 5,000 years of the model run is shown (point), whereas envelopes (shading) represent the range of values simulated over the same time interval (for simulations exhibiting oscillations). MOC, meridional overturning circulation.

conditions—see Methods) was varied from one time slice to the other. Solar luminosity ($1,368 \text{ W m}^{-2}$), atmospheric oxygen concentration (20.95%) and ocean nutrient inventory ($2.1 \mu\text{mol kg}^{-1} \text{ PO}_4$) were kept identical in every model run, and in a first series of simulations (#1), we also kept atmospheric $p\text{CO}_2$ fixed (at 2,240 ppm; see Methods). Hence, we are not aiming to reconstruct the Phanerozoic evolution of climate here (see, for example, refs.^{16,18}) nor necessarily provide a reconstruction of past $[\text{O}_2]$ in the ocean or even recover modern distributions with high fidelity, but, rather, expose the specific impact of changes in continental configuration on gross ocean oxygenation.

Despite assuming both invariant solar constant and $p\text{CO}_2$, substantive variability in climate through the Phanerozoic occurs in the model (Fig. 1b). This is an expected result of sea-level-driven changes in the proportion of absorptive ocean surface versus more reflective land surface^{17,25}, as well as of continental latitudinal distribution, and, in a principal component analysis conducted across all 28 time slices, we find a strong positive correlation between global mean sea-surface temperature (SST) and global ocean surface area (Fig. 1e; $R^2 = 0.585$). Given our assumption of invariant $p\text{O}_2$ (deliberately chosen to expose the role of the continental configuration), we find a relatively straightforward and expected inverse relationship between mean ocean-surface $[\text{O}_2]$ and SST (Fig. 1b,e)—driven primarily by changes in oxygen solubility and modulated by the latitudinal distribution of ocean surface area. Global mean subsurface (around 90–190 m depth in the model) $[\text{O}_2]$ exhibits a more exaggerated temporal evolution (Fig. 1c). Respiration of organic matter exported from the ocean surface now strongly amplifies subsurface oxygen variability (Fig. 1c,e) and introduces new features unconnected to SST changes, such as the approximately $35 \mu\text{mol kg}^{-1}$ decrease from 460 to 400 Ma. This is our first hint of the

importance of changing continental distribution and, hence, large-scale pattern of ocean circulation, which—in the case of subsurface $[\text{O}_2]$ —is by means of changes in the resupply of nutrients to the surface. Even without attempting to simulate a realistic sequence of Phanerozoic climate states (and, hence, changing ocean-surface oxygen solubility), our modelling provides hints to the timing of oceanic anoxic events (OAEs) during the Phanerozoic (Fig. 2 and Extended Data Fig. 2). For instance, seafloor ocean deoxygenation develops in the Palaeo-Tethys during the Permian–Triassic transition (ca. 260 Ma)²⁶ and in the central Atlantic during the Early Cretaceous (ca. 120 Ma)²⁷ and Late Cretaceous (ca. 100 Ma)²⁸. That the Late Devonian OAE (380 Ma)²⁹ and Toarcian OAE (ca. 180 Ma)³⁰ are not captured by our simulations may be a result of the coarse model grid (for the Tethys Ocean during the Toarcian OAE in particular³⁰; Fig. 2 and Extended Data Fig. 2). This could also be interpreted as reflecting the need for a strong perturbation (warming and nutrient-driven increase in primary productivity) at that time to trigger an OAE, as the continental configuration itself is not particularly prone to ocean deoxygenation in our model simulations.

Our unexpected discovery from the numerical modelling is how variable global deep-ocean $[\text{O}_2]$ (calculated as the mean of all benthic grid points in the model below 1,000 m depth) is (Fig. 1d), ranging from $30 \mu\text{mol kg}^{-1}$ (and near fully anoxic) to $178 \mu\text{mol kg}^{-1}$ (a little higher than modern). The early Palaeozoic (541 to 460 Ma) stands out in particular and is characterized by anomalously poor deep seafloor oxygenation (generally less than $45 \mu\text{mol kg}^{-1}$) in the model, with an abrupt increase to $171 \mu\text{mol kg}^{-1}$ at 440 Ma and mostly remaining above $100 \mu\text{mol kg}^{-1}$ thereafter (Fig. 1d). The step change in benthic oxygenation simulated between 460 Ma and 440 Ma is similarly observed using an alternative set of continental reconstructions³¹ (Extended

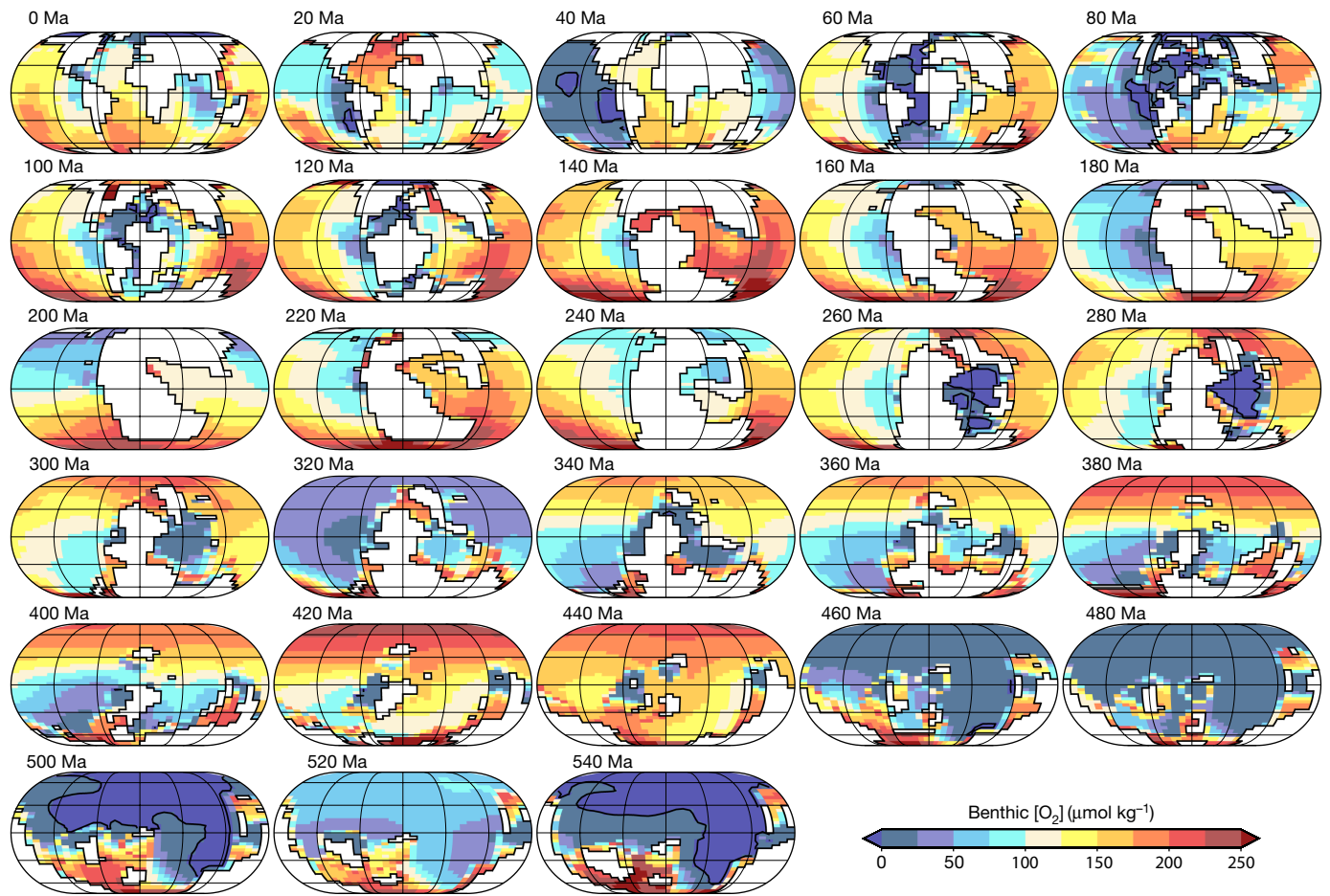


Fig. 2 | Benthic oxygen concentrations for simulations at 2,240 ppm CO₂ (series #1). Eckert IV projection. Emerged continental masses are shaded white. Results are averaged over the last 5,000 years. See Extended Data Fig. 2

for magnified versions of seven panels with redox proxy data points and Extended Data Fig. 3 for the meridional overturning circulation and regions of deep-water formation.

Data Fig. 4). Simulated water age (the mean time since a water parcel was last exposed to the atmosphere) anticorrelates with mean global and benthic [O₂] (Fig. 1d,e), whereas SST and global water age do not correlate (Fig. 1e; $R^2 = 0.001$), pointing to the dominance of a palaeogeographical control on deep-ocean oxygenation.

To further simplify the attribution of causes of benthic [O₂] variability through the Phanerozoic and eliminate global climate change and resulting solubility-driven upper-ocean [O₂] variations as explanatory factors, we carried out a second series of model experiments (#2), in which we kept mean global SST and surface oxygenation largely invariant (Fig. 3). Climate detrending was achieved by varying $p\text{CO}_2$ in the model. Variance in mean benthic [O₂] (Fig. 3d) is now, if anything, even greater than in #1 (Fig. 1d) and the general trend of a poorly oxygenated early Palaeozoic deep ocean still stands. These results confirm that benthic anoxia in the early Palaeozoic ocean results from changes in the deep-ocean circulation in the model, rather than temperature-driven variations in upper-ocean [O₂]. Sensitivity tests demonstrate that global mean temporal trends and spatial oxygenation patterns are largely independent of whether a temperature-dependent (Fig. 1) or fixed remineralization profile (Extended Data Fig. 5) is assumed. Similarly, patterns of benthic [O₂] are only weakly affected by uncertainties in the position of mid-ocean ridges (Extended Data Figs. 6 and 7).

The role of continental configuration in creating conditions of extreme deep-ocean deoxygenation and weakened ventilation (old water mass ages) during the early Palaeozoic (before 440 Ma in series #1 (Fig. 1d) and before 420 Ma in series #2 (Fig. 3d)), arises from

the existence of state transitions in the large-scale circulation of the ocean in the model. Using series #1 as an example, the oldest time slices (540–500 Ma) are characterized by a poorly ventilated seafloor with deep waters forming over the South Pole (Figs. 1d and 2 and Extended Data Fig. 8a). At 480 and 460 Ma, the ocean circulation oscillates between the previous poorly ventilated state and a better-ventilated state, the latter state subsequently becoming stabilized at 440 Ma by further tectonic rearrangement (Figs. 1d and 2 and Extended Data Fig. 8a). Of course, the differences in the two simulation series illustrate that the climate state also influences the ocean circulation regimes (contrast Figs. 1 and 3; see also Extended Data Figs. 8 and 9). Several lines of evidence suggest that these state transitions are a robust characteristic of the early Palaeozoic, at least in the cGENIE model. Indeed, further simulations conducted using idealized land-sea masks show that these state transitions may be a characteristic feature of continental configurations with one pole free of land (Extended Data Fig. 10 and Methods), such as the one of the early Palaeozoic (Fig. 2), and a similar reorganization of the global ocean circulation has previously been shown to best explain the expansion of seafloor anoxia during Late Ordovician glaciation (Extended Data Fig. 10 and ref. ²¹).

The occurrence of climate-driven state transitions in ocean circulation and oxygenation is well established in the context of changes in Atlantic and Pacific basin meridional overturning since the last glacial maximum (21 ka)^{32,33}. By contrast, the potential for ocean state transitions in deeper time has received much less attention but is no less important (see, for example, ref. ²¹). We also have good reason to

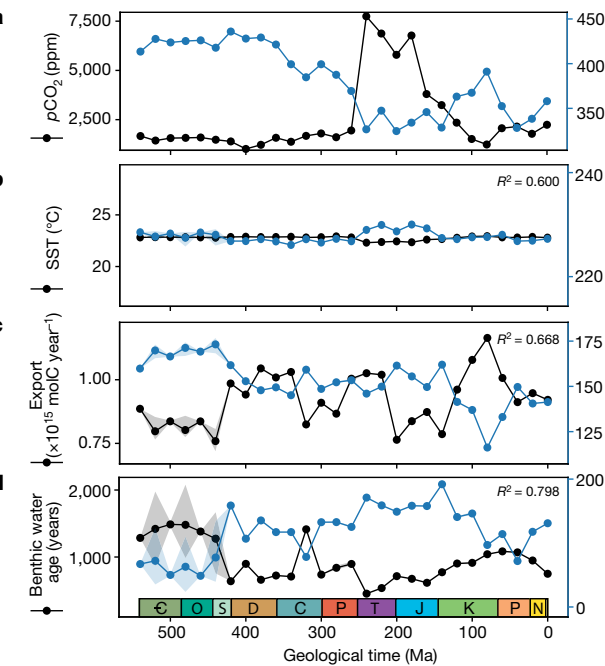


Fig. 3 | Earth system model results for simulations in which we varied $p\text{CO}_2$ to approximately ‘correct’ for the palaeogeographical impacts on climate (series #2). Panels a–d and panel description as per Fig. 1. Note that, in this series of experiments, surface oxygenation and mean global SST (panel b) are largely invariant.

conclude that the occurrence of oscillatory ocean circulation modes is not an artefact of the particular model used here and may occur as a transitional regime between different stable steady states (Extended Data Fig. 10). For instance, oscillations have previously been identified in both (ocean-only) 3D ocean circulation models^{34,35} and 3D ocean circulation models coupled to simplified representations of atmospheric dynamics (Earth system models of intermediate complexity)^{36,37}. Non-steady solutions in volume-integrated ocean temperature are also hinted at in several recent fully coupled general circulation model (GCM) simulations under specific continental configurations and climate states¹⁶. Further work conducted using higher-resolution Earth system models, such as the Coupled Model Intercomparison Project phase 6 generation, will be important to distinguish robust from model-dependent modes of ocean circulation, although identifying the boundary conditions giving rise to oscillatory modes will be computationally challenging.

Our finding of a fundamental decoupling of subsurface and benthic $[\text{O}_2]$ during the Phanerozoic (Fig. 1e; $R^2 = 0.001$) implies that no simple relationship exists during the Phanerozoic among the concentrations of oxygen in the atmosphere, the subsurface ocean and at the seafloor. Furthermore, the highly non-linear nature of the system means that even very minor changes in continental configuration (for example, contrast 460 versus 440 Ma; Fig. 2) can induce pronounced reorganizations of large-scale circulation and, hence, ocean oxygenation and, similarly, confound any predictable relationship between changes in atmospheric $p\text{CO}_2$ (and climate) and ocean oxygenation. This has implications not only for how we interpret deep-ocean redox proxy records and specifically proxies for the global areal extent of seafloor anoxia⁵ (such as, $\delta^{238}\text{U}$ (ref.¹²) and $\delta^{98}\text{Mo}$ (ref.⁹)) but also how we understand the underlying controls on ocean anoxia and infer changes in atmospheric composition. For instance, Stolper and Keller³⁸ analysed the ratio of Fe^{3+} to total Fe ($\text{Fe}^{3+}/\Sigma\text{Fe}$) in hydrothermally altered basalts formed in ocean basins to quantitatively reconstruct deep-ocean $[\text{O}_2]$ over the past 3,500 Myr. Their results indicate that the deep ocean became oxygenated only in the Phanerozoic and probably not until the late Palaeozoic

(<420 Myr). Our simulations support the vision of a poorly oxygenated early Palaeozoic ocean^{4,5,38} (until ca. 440 Ma in the model; see Figs. 1d and 3d). However, although $\text{Fe}^{3+}/\Sigma\text{Fe}$ data are interpreted as reflecting an increase in atmospheric oxygen concentrations³⁸, our Earth system simulations, by contrast, suggest that deep-ocean oxygenation around 440–420 Ma could have been a consequence of continental rearrangement and concomitant changes in ocean circulation and ventilation. The implication is that early Phanerozoic atmospheric $p\text{O}_2$ need not have been appreciably lower than modern, which aligns with the measurements of atmospheric oxygen trapped in fluid–gas inclusions of halite³⁹. Furthermore, the step changes in early Palaeozoic seafloor oxygenation are indicative of bistability between deep-ocean circulation states; that is, for certain continental configurations, multiple advection and convection patterns will co-exist (what is observed depends on the initial conditions of the simulation). Switches between such states could provide an explanation for the swings⁵ in early Palaeozoic global anoxia extent documented on the grounds of $\delta^{238}\text{U}$ (refs.^{40–42}) and $\delta^{98}\text{Mo}$ (refs.^{41,43}). Uncertainties in both the model and geological data preclude us from determining if our simulated scenario may have actually taken place in the geological past, and we recognize that continental rearrangement is also not exclusive of secular variation in other drivers of ocean anoxia, such as atmospheric oxygen, ocean nutrient inventory and global warming^{13,19,21,26}. That said, and despite our idealized boundary conditions and invariant atmospheric chemistry, there are shared temporal trends (albeit with different timings and interval durations) with recent I/Ca-based oxygen proxy compilations¹³, namely, low oxygenation in the early and late Palaeozoic with a high during the Devonian, and peak values occurring before late Cenozoic cooling.

Finally, our results have implications for the evolution of marine animal ecosystems through the Phanerozoic. If kyr-scale oscillations in ocean oxygenation were a characteristic feature of early Palaeozoic oceans, as supported by the high-resolution Mo record of ref.⁴⁴ and our modelling (Extended Data Fig. 8), this would lend support to arguments linking the progressive (here, palaeogeographical) stabilization of a steady-state Earth system to decreasing extinction rates through the Phanerozoic^{6,45}.

Online content

Any methods, additional references, Nature Research reporting summaries, source data, extended data, supplementary information, acknowledgements, peer review information; details of author contributions and competing interests; and statements of data and code availability are available at <https://doi.org/10.1038/s41586-022-05018-z>.

1. Payne, J. L. et al. Two-phase increase in the maximum size of life over 3.5 billion years reflects biological innovation and environmental opportunity. *Proc. Natl Acad. Sci. USA* **106**, 24–27 (2009).
2. Cole, D. B. et al. On the co-evolution of surface oxygen levels and animals. *Geobiology* **18**, 260–281 (2020).
3. Sperling, E. A., Knoll, A. H. & Gireg, P. R. The ecological physiology of Earth’s second oxygen revolution. *Annu. Rev. Ecol. Evol. Syst.* **46**, 215–235 (2015).
4. Krause, A. J. et al. Stepwise oxygenation of the Paleozoic atmosphere. *Nat. Commun.* **9**, 4081 (2018).
5. Tostevin, R. & Mills, B. J. Reconciling proxy records and models of Earth’s oxygenation during the Neoproterozoic and Palaeozoic. *Interface Focus* **10**, 20190137 (2020).
6. Kocsis, Á. T., Reddin, C. J., Alroy, J. & Kiessling, W. The R package divDyn for quantifying diversity dynamics using fossil sampling data. *Methods Ecol. Evol.* **10**, 735–743 (2019).
7. Penn, J. L., Deutsch, C., Payne, J. L. & Sperling, E. A. Temperature-dependent hypoxia explains biogeography and severity of end-Permian marine mass extinction. *Science* **362**, eaat1327 (2018).
8. Edwards, C. T., Saltzman, M. R., Royer, D. L. & Fike, D. A. Oxygenation as a driver of the Great Ordovician Biobrevification Event. *Nat. Geosci.* **10**, 925–929 (2017).
9. Dahl, T. W., Hammarlund, E. U. & Anbar, A. D. Devonian rise in atmospheric oxygen correlated to the radiations of terrestrial plants and large predatory fish. *Proc. Natl Acad. Sci.* **107**, 17911–17915 (2010).
10. Zou, C. et al. Ocean euxinia and climate change “double whammy” drove the Late Ordovician mass extinction. *Geology* **46**, 535–538 (2018).
11. Bond, D., Wignall, P. B. & Racki, G. Extent and duration of marine anoxia during the Frasnian–Famennian (Late Devonian) mass extinction in Poland, Germany, Austria and France. *Geol. Mag.* **141**, 173–193 (2004).

12. Lau, K. V. et al. Marine anoxia and delayed Earth system recovery after the end-Permian extinction. *Proc. Natl Acad. Sci.* **113**, 2360–2365 (2016).
13. Lu, W. et al. Late inception of a resiliently oxygenated upper ocean. *Science* **5**, eaar5372 (2018).
14. Sperling, E. A. et al. A long-term record of early to mid-Paleozoic marine redox change. *Sci. Adv.* **7**, eabf4382 (2021).
15. Lenton, T. M. Earliest land plants created modern levels of atmospheric oxygen. *Proc. Natl Acad. Sci.* **113**, 9704–9709 (2016).
16. Valdes, P., Scotese, C. & Lunt, D. Deep ocean temperatures through time. *Clim. Past* **17**, 1483–1506 (2021).
17. Farnsworth, A. et al. Climate sensitivity on geological timescales controlled by nonlinear feedbacks and ocean circulation. *Geophys. Res. Lett.* **46**, 9880–9889 (2019).
18. Scotese, C. R., Song, H., Mills, B. J. & van der Meer, D. G. Phanerozoic paleotemperatures: the earth's changing climate during the last 540 million years. *Earth Sci. Rev.* **215**, 103503 (2021).
19. Monteiro, F. M., Pancost, R. D., Ridgwell, A. & Donnadieu, Y. Nutrients as the dominant control on the spread of anoxia and euxinia across the Cenomanian-Turonian oceanic anoxic event (OAE2): model-data comparison. *Paleoceanography* **27**, PA4209 (2012).
20. Ridgwell, A. et al. Marine geochemical data assimilation in an efficient Earth system model of global biogeochemical cycling. *Biogeosciences* **4**, 87–104 (2007).
21. Pohl, A. et al. Vertical decoupling in Late Ordovician anoxia due to reorganization of ocean circulation. *Nat. Geosci.* **14**, 868–873 (2021).
22. Ward, B. A. et al. EcoGENIE 1.0: plankton ecology in the cGENIE Earth system model. *Geosci. Model Dev.* **11**, 4241–5267 (2018).
23. Crichton, K. A., Wilson, J. D., Ridgwell, A. & Pearson, P. N. Calibration of temperature-dependent ocean microbial processes in the cGENIE.muffin (v0.9.13) Earth system model. *Geosci. Model Dev.* **14**, 125–149 (2021).
24. Scotese, C. R. & Wright, N. PALEOMAP Paleodigital Elevation Models (PaleoDEMs) for the Phanerozoic. PALEOMAP Project. <https://www.earthbyte.org/paleodem-resource-scotese-and-wright-2018/> (2018).
25. Pohl, A. et al. Quantifying the paleogeographic driver of Cretaceous carbonate platform development using paleoecological niche modeling. *Palaeogeogr. Palaeoclimatol. Palaeoecol.* **514**, 222–232 (2019).
26. Hülse, D. et al. End-Permian marine extinction due to temperature-driven nutrient recycling and euxinia. *Nat. Geosci.* **14**, 862–867 (2021).
27. Baudin, F. & Riquier, L. The late Hauerian Faraoni 'oceanic anoxic event': an update. *Bull. Soc. Géol. Fr.* **185**, 359–377 (2014).
28. Laugié, M. et al. Exploring the impact of Cenomanian paleogeography and marine gateways on oceanic oxygen. *Paleoceanogr. Paleoclimatol.* **36**, e2020PA004202 (2021).
29. De Vleeschouwer, D. et al. Timing and pacing of the Late Devonian mass extinction event regulated by eccentricity and obliquity. *Nat. Commun.* **8**, 2268 (2017).
30. Ruvalcaba Baroni, I. et al. Ocean circulation in the Toarcian (Early Jurassic): a key control on deoxygenation and carbon burial on the European Shelf. *Paleoceanogr. Paleoclimatol.* **33**, 994–1012 (2018).
31. Torsvik, T. H. BugPlates: Linking Biogeography and Palaeogeography (2009).
32. Ferreira, D., Marshall, J., Ito, T. & McGee, D. Linking glacial-interglacial states to multiple equilibria of climate. *Geophys. Res. Lett.* **45**, 9160–9170 (2018).
33. Jaccard, S. L. & Galbraith, E. D. Large climate-driven changes of oceanic oxygen concentrations during the last deglaciation. *Nat. Geosci.* **5**, 151–156 (2012).
34. Weijer, W. & Dijkstra, H. A. Multiple oscillatory modes of the global ocean circulation. *J. Phys. Oceanogr.* **33**, 2197–2213 (2003).
35. Sirkes, Z. & Tziperman, E. Identifying a damped oscillatory thermohaline mode in a general circulation model using an adjoint model. *J. Phys. Oceanogr.* **31**, 2297–2306 (2001).
36. Meissner, K. J., Eby, M., Weaver, A. J. & Saenko, O. A. CO₂ threshold for millennial-scale oscillations in the climate system: Implications for global warming scenarios. *Clim. Dyn.* **30**, 161–174 (2008).
37. Haarsma, R. J., Opsteegh, J. D., Selten, F. M. & Wang, X. Rapid transitions and ultra-low frequency behaviour in a 40 kyr integration with a coupled climate model of intermediate complexity. *Clim. Dyn.* **17**, 559–570 (2001).
38. Stolper, D. A. & Keller, C. B. A record of deep-ocean dissolved O₂ from the oxidation state of iron in submarine basalts. *Nature* **553**, 323–327 (2018).
39. Brand, U. et al. Atmospheric oxygen of the Paleozoic. *Earth Sci. Rev.* **216**, 103560 (2021).
40. Dahl, T. W. et al. Reorganisation of Earth's biogeochemical cycles briefly oxygenated the oceans 520 Myr ago. *Geochem. Perspect. Lett.* **3**, 210–220 (2019).
41. Wei, G. Y. et al. Global marine redox evolution from the late Neoproterozoic to the early Paleozoic constrained by the integration of Mo and U isotope records. *Earth Sci. Rev.* **214**, 103506 (2021).
42. Wei, G. Y. et al. Marine redox fluctuation as a potential trigger for the Cambrian explosion. *Geology* **46**, 587–590 (2018).
43. Kendall, B. et al. Uranium and molybdenum isotope evidence for an episode of widespread ocean oxygenation during the late Ediacaran Period. *Geochim. Cosmochim. Acta* **156**, 173–193 (2015).
44. Dahl, T. W. et al. Brief oxygenation events in locally anoxic oceans during the Cambrian solves the animal breathing paradox. *Sci Rep.* **9**, 11669 (2019).
45. Payne, J. L., Bachan, A., Heim, N. A., Hull, P. M. & Knope, M. L. The evolution of complex life and the stabilization of the Earth system. *Interface Focus* **10**, 20190106 (2020).

Publisher's note Springer Nature remains neutral with regard to jurisdictional claims in published maps and institutional affiliations.

© The Author(s), under exclusive licence to Springer Nature Limited 2022

Article

Methods

Description of the model

cGENIE²⁰—an ‘Earth system model of intermediate complexity’—is based around a 3D ocean circulation model, which—for speed—is coupled to a 2D energy–moisture balance atmospheric component. We configured the model on a 36×36 equal-area grid with 16 unevenly spaced vertical levels to a maximum depth of 5,500 m in the ocean. The cycling of carbon and associated tracers in the ocean is based on a single (phosphate) nutrient limitation of biological productivity accounting for plankton ecology based on refs. ^{22,46}, but adopts the Arrhenius-type temperature-dependent scheme for the remineralization of organic matter exported to the ocean interior of ref. ²³. We further modify the ecological model of ref. ²² to account for limitation of productivity under sea ice, rescale the global mean annual C/P ratio of exported particulate organic matter to match that of the standard model (106)⁴⁷, and only diagnose the ocean-surface mixed-layer depth for calculating light attenuation rather than entrain this into the physical circulation. We include a sulphate (SO_4^{2-}) tracer as an electron acceptor in the model in addition to dissolved oxygen, such that when $[\text{O}_2]$ starts to approach zero, sulphate reduction occurs in association with the remineralization of organic matter. The hydrogen sulphide (H_2S) created is transported by means of ocean circulation and oxidized in the presence of O_2 to re-form sulphate. Note that we do not include a nitrogen cycle (and, hence, nitrate reduction) nor methanogenesis in our model tracer configuration. See refs. ^{48,49} for details of the overall ocean redox scheme.

Despite its low spatial resolution, cGENIE satisfactorily simulates first-order ocean $[\text{O}_2]$ spatial patterns and values for the present-day ocean when configured with pre-industrial boundary conditions such as 278 ppm CO_2 (Extended Data Fig. 1 and ref. ²⁰), as well as in the geological past^{19,21}. For instance, simulations for Oceanic Anoxic Event 2 conducted using cGENIE (ref. ¹⁹, their Fig. 2f,g) compare well with simulations conducted using the more complex model IPSL-CM5A2 (ref. ²⁸, their Fig. 10), in terms of both global extent of anoxia and response to gateway alteration.

Description of the numerical experiments

We adopted the (flat-bottomed) Phanerozoic continental reconstructions of ref. ²⁴ but substituted the deep-ocean bathymetry of ref. ⁵⁰ when available (140–0 Ma) to account for mid-ocean ridges. To specifically quantify the impact of palaeogeographical evolution, we kept solar luminosity ($1,368 \text{ W m}^{-2}$), atmospheric oxygen concentrations (20.95%) and ocean nutrient inventory ($2.1 \mu\text{mol kg}^{-1} \text{ PO}_4$) invariant. We used a null eccentricity–minimum obliquity orbital configuration, which provides an equal mean annual insolation to both hemispheres with minimum seasonal contrasts. Atmospheric CO_2 concentration was kept fixed in series #1 (2,240 ppm) but varied in series #2 to approximately ‘correct’ for the palaeogeographical impacts on climate. These forcing combinations ensured that simulated ocean temperatures are on the right order of magnitude compared with the Phanerozoic proxy-derived trend¹⁸. The mean Phanerozoic tropical (25° S – 25° N) SST is 29.67° C (standard deviation 1.88° C) in series #1 (mean of 29.39° C and standard deviation of 0.45° C in series #2) compared with a mean of 28.1° C (standard deviation 2.51° C) in the data compilation¹⁸.

To generate the physical atmospheric boundary conditions required by cGENIE for each different continental configuration, we ran FOAM⁵¹ GCM experiments for 2–3 kyr, until deep-ocean temperature equilibrium. We then derived the 2D wind speed and wind stress, and 1D zonally averaged albedo forcing fields required by the cGENIE model, using the ‘muffingen’ open-source software (<https://doi.org/10.5281/zenodo.5500687>), following the methods used in ref. ⁵².

Simulations were initialized with a sea-ice-free ocean and homogeneous temperature and salinity in the ocean (5° C and 33.9‰, respectively) and integrated for a total of 20,000 years. Data are presented reflecting either the average over the last 5,000 years of the simulation

(for example, Fig. 2) or the mean and range of any oscillation over the last 5,000 years (for example, Figs. 1 and 3), as detailed in the figure captions.

Principal component analysis

Principal component analyses of Fig. 1 and Extended Data Fig. 5 were performed using, for each variable, the mean value simulated over the last 5,000 years of the model simulations. For each variable, a total of 28 values was thus obtained (one value for each of the 28 time slices, from 540 Ma to 0 Ma every 20 Myr). We considered 13 variables: surface $[\text{O}_2]$, subsurface $[\text{O}_2]$, benthic $[\text{O}_2]$, global $[\text{O}_2]$, global water age, benthic water age, sea-surface temperature (‘SST’), benthic temperature, $p\text{CO}_2$, meridional overturning circulation maximum (‘MOC max’) and minimum (‘MOC min’), export production (‘export’; that is, the flux of organic carbon produced in the ocean photic zone by primary producers that is not recycled (remineralized) before sinking deeper in the water column) and total ocean area. The principal component analysis was conducted using the ‘PCA’ function of the R package ‘FactoMineR’⁵³ and the first two axes/principal components were represented (capturing about 68% of the variance in both cases). The objective here is not to provide a thorough principal component analysis but rather to (1) confirm the robustness of the correlations illustrated in the form of time series and R^2 in the other panels of Fig. 1 and Extended Data Fig. 5 and (2) provide information on the correlation (or not) of further key variables in a synthetic and graphical manner.

More discussion on ocean circulation regimes

Most of the simulations in Extended Data Fig. 8a,b show that ocean dynamics obtain stable steady-state solutions. However, among these are cases in which the system overshoots (for example, compare 0 Ma and 120 Ma in Extended Data Fig. 8a) before approaching a steady-state solution. This may imply the presence of an oscillatory mode, in agreement with the linear stability analysis of low-resolution GCM steady states under present-day conditions^{34,35}. The simulations in Extended Data Fig. 8 show that, depending on changes to continental configuration, the steady-state solutions can lose stability, resulting in stable oscillations. It is known that, under certain climate conditions, advective feedbacks in the ocean circulation can destabilize the steady state⁵⁴. Simulations for 540 Ma and 500 Ma in Extended Data Fig. 8a,b, respectively, are cases of steady-state solutions with oscillatory modes that are linearly stable, but only weakly stable, resulting in clear examples of damped oscillations. Because the frequencies of the damped and self-sustained oscillations (500 and 520 Ma in Extended Data Fig. 8b, respectively) are very similar, the transition could represent a Hopf bifurcation, resulting in self-sustained oscillations (characterized by fluctuations in circulation pattern and strength) around an unstable steady state.

To better understand the model behaviour and, ultimately, the nature of the state transitions in the global ocean circulation, we conducted further cGENIE simulations using two contrasting, idealized continental configurations featuring either a latitudinal strip of land from the North Pole to the Southern Hemisphere mid-latitudes (‘Drake world’⁵⁵) or a strip of land extending from the North Pole to the South Pole (‘ridge world’⁵⁵) (Extended Data Fig. 10). Drake world, with a pole free of land (that is, purely oceanic at all longitudes), schematically represents the continental configuration of the early Palaeozoic (or a high-latitude circumpolar path such as in the late Cenozoic), whereas ridge world represents an early-Mesozoic-like continental arrangement with land masses present from the North Pole to the South Pole (see Fig. 2).

With Drake world, at low $p\text{CO}_2$ levels, deep-water formation takes place at the North Pole, where a slightly higher hemispherical fraction of land cover with lower thermal inertia favours winter cooling over the surrounding ocean and convection (label 1 in Extended Data Fig. 10a,b). As atmospheric CO_2 is steadily increased across a series of experiments, the onset of a first set of oscillations, between $\times 5.5$ and

$\times 7.5$ CO₂ (label 2), marks the development of a new equilibrium that stabilizes in the subsequent stable steady state at around $\times 8.25$ CO₂ (label 3). Then, a new set of oscillations, from $\times 9$ to $\times 9.75$ CO₂, marks another step towards the weakening of the deep-water formation over the North Pole and strengthening over the South Pole (label 4). A third stable equilibrium finally stabilizes above $\times 10.75$ CO₂ (label 5). Each set of oscillations thus marks the shift to a new regime of steady-state circulation and the ultimate result is a shift in the locus of deep-water formation from the North Pole (with land barriers) to the South Pole (oceanic) in response to global warming from $\times 4$ to $\times 16$ CO₂. A comparable (but latitudinally reversed) behaviour was previously observed by Pohl et al.²¹ for the latest Ordovician. In response to global warming (their Fig. 4e–i; see also Extended Data Fig. 10c), the locus of deep-water formation shifts in their simulations from the South Pole (with lands) to the North Pole (oceanic). This is very similar to the change in ocean circulation simulated between 460 Ma and 440 Ma in simulation series #1 (Fig. 2), although the state transition here involves continental rearrangement in addition to global warming (global SST increases from 24.1 °C at 460 Ma to 24.38 °C at 440 Ma). No similar state transition is observed using the ridge world configuration (Extended Data Fig. 10a).

Code availability

The version of the cGENIE code used in this paper is tagged as release v0.9.31 and is available at <https://doi.org/10.5281/zenodo.6823664>. Necessary boundary condition files are included as part of the code release. Configuration files for the specific experiments presented in the paper can be found in the installation subdirectory: `genie-userconfigs/PUBS/published/Pohl_et_al.2022`. Details of the experiments, plus the command line needed to run each one, are given in the `readme.txt` file in that directory. A manual describing code installation, basic model configuration and an extensive series of tutorials is provided (<https://doi.org/10.5281/zenodo.5500696>). The FOAM output is hosted on Zenodo (<https://doi.org/10.5281/zenodo.5780096>).

46. Wilson, J. D., Monteiro, F. M., Schmidt, D. N., Ward, B. A. & Ridgwell, A. Linking marine plankton ecosystems and climate: a new modeling approach to the warm early Eocene climate. *Paleoceanogr. Paleoceanogr.* **33**, 1439–1452 (2018).
47. Cao, L. et al. The role of ocean transport in the uptake of anthropogenic CO₂. *Biogeosciences* **6**, 375–390 (2009).
48. Reinhard, T. C. et al. Oceanic and atmospheric methane cycling in the cGENIE Earth system model – release v0.9.14. *Geosci. Model Dev.* **13**, 5687–5706 (2020).
49. van de Velde, S. J., Hülse, D., Reinhard, C. T. & Ridgwell, A. Iron and sulfur cycling in the cGENIE.muffin Earth system model (v0.9.21). *Geosci. Model Dev.* **14**, 2713–2745 (2021).

50. Müller, R. D., Sdrolias, M., Gaina, C., Steinberger, B. & Heine, C. Long-term sea-level fluctuations driven by ocean basin dynamics. *Science* **319**, 1357–1362 (2008).
51. Jacob, R. L. *Low Frequency Variability in a Simulated Atmosphere-Ocean System*. Thesis, Univ. Wisconsin (1997).
52. Crichton, K. A., Ridgwell, A., Lunt, D., Farnsworth, A. & Pearson, P. Data-constrained assessment of ocean circulation changes since the middle Miocene in an Earth system model. *Clim. Past* **17**, 2223–2254 (2021).
53. Lê, S., Josse, J. & Husson, F. FactoMineR: an R package for multivariate analysis. *J. Stat. Softw.* **25**, 1–18 (2008).
54. Weijer, W. et al. Stability of the Atlantic Meridional Overturning Circulation: a review and synthesis. *J. Geophys. Res. Oceans* **124**, 5336–5375 (2019).
55. Ferreira, D., Marshall, J. & Campin, J. M. Localization of deep water formation: role of atmospheric moisture transport and geometrical constraints on ocean circulation. *J. Clim.* **23**, 1456–1476 (2010).
56. Garcia, H. E. et al. *World Ocean Atlas 2018, Volume 3: Dissolved Oxygen, Apparent Oxygen Utilization, and Dissolved Oxygen Saturation* (National Oceanic and Atmospheric Administration, 2019).
57. Marsh, R. et al. Bistability of the thermohaline circulation identified through comprehensive 2-parameter sweeps of an efficient climate model. *Clim. Dyn.* **23**, 761–777 (2004).
58. DeVries, T. & Holzer, M. Radiocarbon and helium isotope constraints on deep ocean ventilation and mantle-³He sources. *J. Geophys. Res. Oceans* **124**, 3036–3057 (2019).
59. Song, H. et al. The onset of widespread marine red beds and the evolution of ferruginous oceans. *Nat. Commun.* **8**, 399 (2017).
60. Melchin, M. J., Mitchell, C. E., Holmden, C. & Štorch, P. Environmental changes in the Late Ordovician–early Silurian: review and new insights from black shales and nitrogen isotopes. *Geol. Soc. Am. Bull.* **125**, 1635–1670 (2013).
61. Pohl, A., Nardin, E., Vandenbroucke, T. R. A. & Donnadieu, Y. High dependence of Ordovician ocean surface circulation on atmospheric CO₂ levels. *Palaeogeogr. Palaeoclimatol. Palaeoecol.* **458**, 39–51 (2016).
62. Meyer, K. M., Ridgwell, A. & Payne, J. L. The influence of the biological pump on ocean chemistry: implications for long-term trends in marine redox chemistry, the global carbon cycle, and marine animal ecosystems. *Geobiology* **14**, 207–219 (2016).

Acknowledgements We thank J. Mossinger for editorial handling. This project has received financing from the European Union's Horizon 2020 research and innovation programme under Marie Skłodowska-Curie grant agreement no. 838373. Calculations were partly performed using HPC resources from DNUM CCUB (Centre de Calcul de l'Université de Bourgogne). A.R. acknowledges support from NSF grants 1736771 and EAR-2121165, as well as from the Heising-Simons Foundation. This is a contribution to UNESCO project IGCP 735 'Rocks and the Rise of Ordovician Life (Rocks n' ROL)'.

Author contributions A.P. and A.R. designed the study and wrote the manuscript, with input from all co-authors. A.P. and A.R. conducted the FOAM and cGENIE experiments. A.P., A.R. and A.K. led the analysis of the model results. C.R.S. produced the continental reconstructions.

Competing interests The authors declare no competing interests.

Additional information

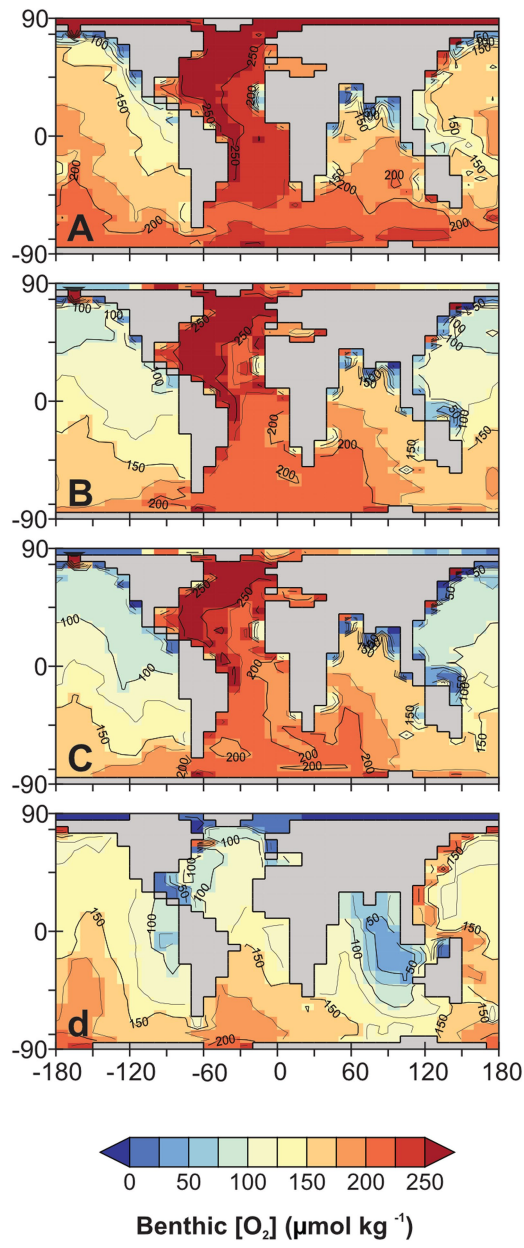
Supplementary information The online version contains supplementary material available at <https://doi.org/10.1038/s41586-022-05018-z>.

Correspondence and requests for materials should be addressed to Alexandre Pohl.

Peer review information *Nature* thanks Tais Dahl, Shuhai Xiao, Sabin Zahirovic and the other, anonymous, reviewer(s) for their contribution to the peer review of this work. Peer reviewer reports are available.

Reprints and permissions information is available at <http://www.nature.com/reprints>.

Article



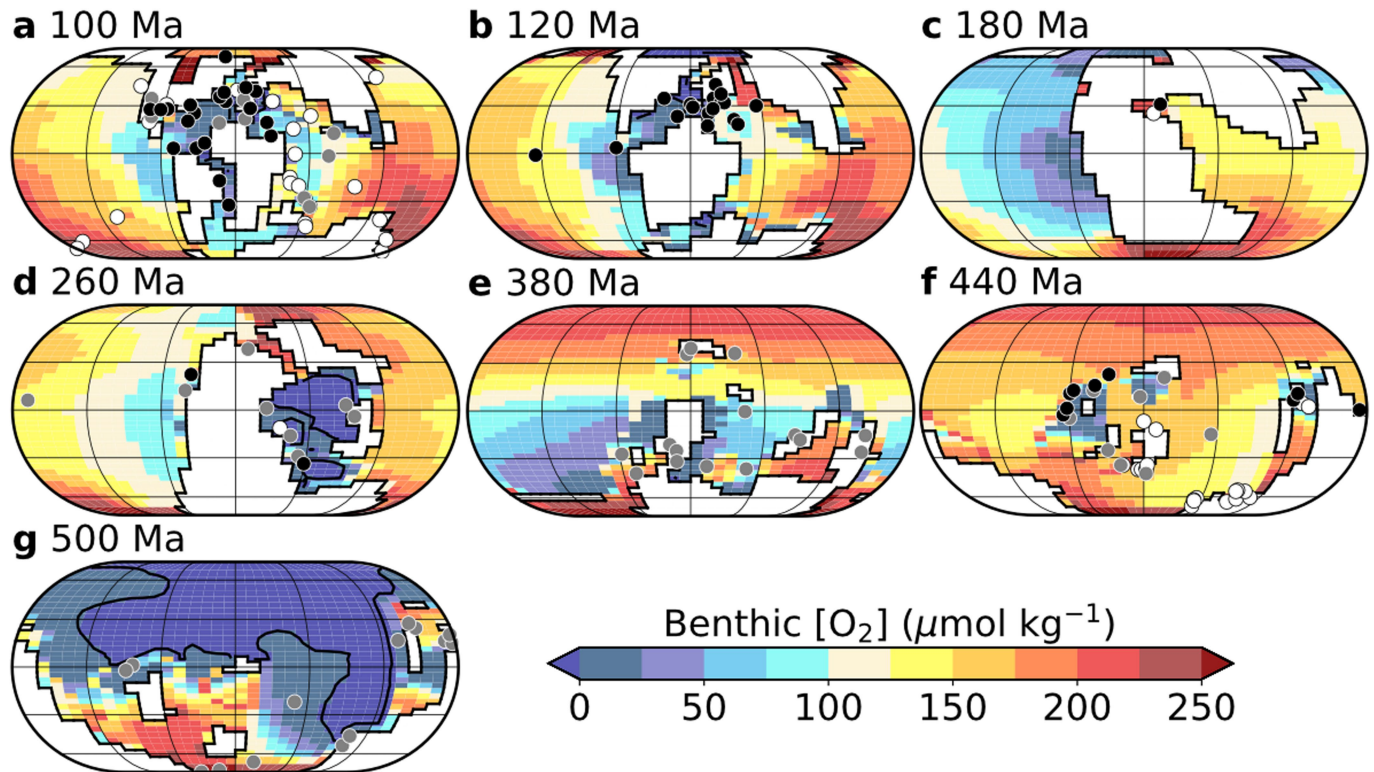
Extended Data Fig. 1 | See next page for caption.

Extended Data Fig. 1 | Comparison of modern observations of seafloor

[O₂] with the cGENIE model. Results are shown for different (modern) continental grids, boundary conditions and biogeochemical cycling parameterization assumptions. Projection is equal-area rectangular and the colour scale is chosen to approximately match that in Fig. 2. **a**, Present-day distribution of [O₂] globally at the seafloor, for which we re-grid the World Ocean Atlas 2018 (ref. ⁵⁶) data to the modern continental grid of ref. ⁴⁷ and show the oxygen concentration in the deepest model grid point. Apparent is both the production and southward propagation (via North Atlantic Deep Water (NADW)) of highly oxygenated waters from the North Atlantic and oxygenated deep-water production and mixing around Antarctica. **b**, Benthic [O₂] distribution for the ‘standard’ modern ocean circulation of ref. ⁴⁷ run at 278 ppm CO₂, plus simplified biological export scheme. The large-scale patterns of benthic [O₂] are reasonably reproduced, with the exception of too weak mixing of oxygen around the Southern Ocean, itself caused by a weak simulated Antarctic Circumpolar Current (ACC) and the difficulty in adequately representing the Drake Passage at this resolution. The slightly too low compared with observations values in the North Pacific is a further consequence of this. **c**, Test of substituting the simplified biological export scheme of ref. ⁴⁷ with the explicit ecosystem model used here in the Phanerozoic series of simulations (but still at 278 ppm CO₂). The slightly

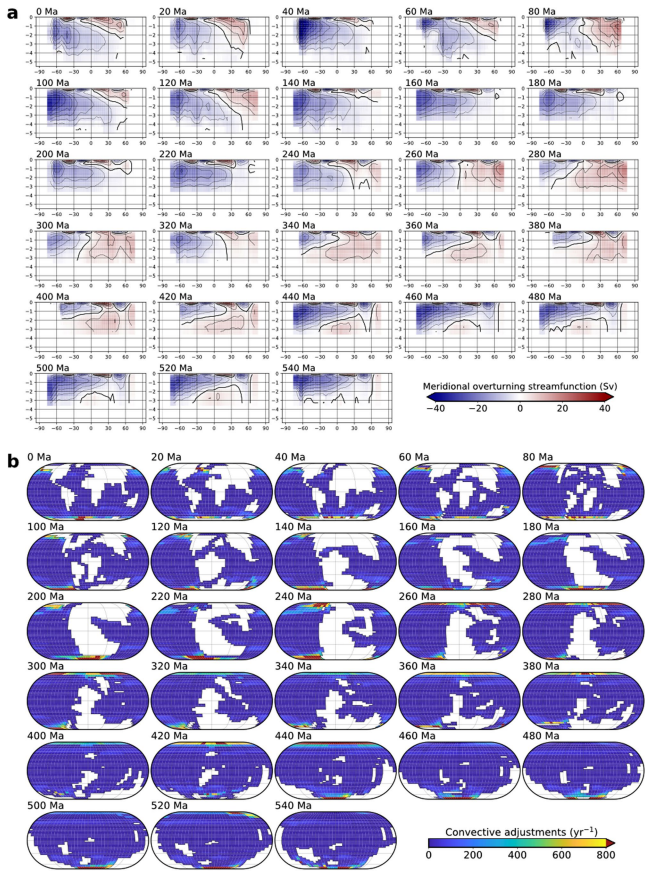
greater export simulated by the ecological model reduces benthic [O₂] by about 10–20 μmol kg⁻¹ while leaving the large-scale patterns largely unaltered. **d**, Deep-sea oxygenation in the 0 Ma Phanerozoic simulation (as per Fig. 2, 0 Ma) run at 2,240 ppm CO₂. Without flux adjustment applied in the simplified cGENIE 2D EMBM atmosphere (see ref. ⁵⁷), there is virtually no NADW, explaining the relatively poor and south-to-north oxygenation of the Atlantic. The Indian Ocean is also too poorly oxygenated, although the general pattern in the Pacific is reproduced. There are several main reasons for this model–data mismatch. First, directly re-gridding from a relatively coarse resolution GCM (FOAM) creates a highly restricted and shallow Drake Passage (Extended Data Fig. 7a, 0 Ma), precluding a strong ACC forming. More pertinently, the Phanerozoic simulation series (Fig. 2) are all run at 2,240 ppm. The resulting much-warmer-than-modern ocean is associated with the absence of any sea-ice formation and lower seawater oxygen solubility, probably explaining at least some of the spatial pattern and much of the lower global mean [O₂] inventory (Extended Data Fig. 8a, 0 Ma). In terms of ventilation and water mass idealized mean age (not shown), the Atlantic, lacking an Atlantic MOC is far too old, whereas the Indian and Pacific oceans are similar to the inverse modelling of ref. ⁵⁸, despite the aforementioned issues with the Drake Passage and that the 0 Ma simulation is run at 2,240 ppm CO₂.

Article



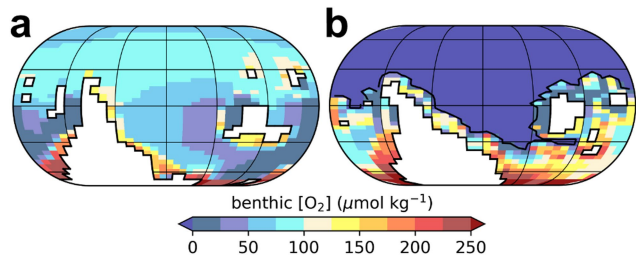
Extended Data Fig. 2 | Selected redox proxy data versus the corresponding model oxygenation realization. Benthic oxygen concentrations for simulations at 2,240 ppm CO₂ (series #1). Eckert IV projection. Emerged continental masses are shaded white. Results are averaged over the last 5,000 years. Black (white) dots represent anoxic (oxic) conditions and grey points represent possible or intermittent anoxia, for 100 Ma after ref. ²⁸, for 120 Ma after ref. ²⁷, for 180 Ma after ref. ³⁰, for 260 Ma after ref. ²⁶, for 380 and 500 Ma after ref. ⁵⁹ and for 440 Ma after ref. ⁶⁰. These time slices have been

chosen to represent regularly spaced periods during the Phanerozoic, typified by OAEs. The last 100 Myr are deliberately omitted because (1) the ocean is, overall, well oxygenated during this time interval and (2) our constant boundary conditions (deliberately chosen to isolate the role of tectonics from climate, see main text) do not (and, indeed, do not intend to) reproduce the pronounced cooling trend through the Cenozoic (especially from Early Eocene Climatic Optimum (ca. 50 Ma) onwards), precluding direct model–data comparison.

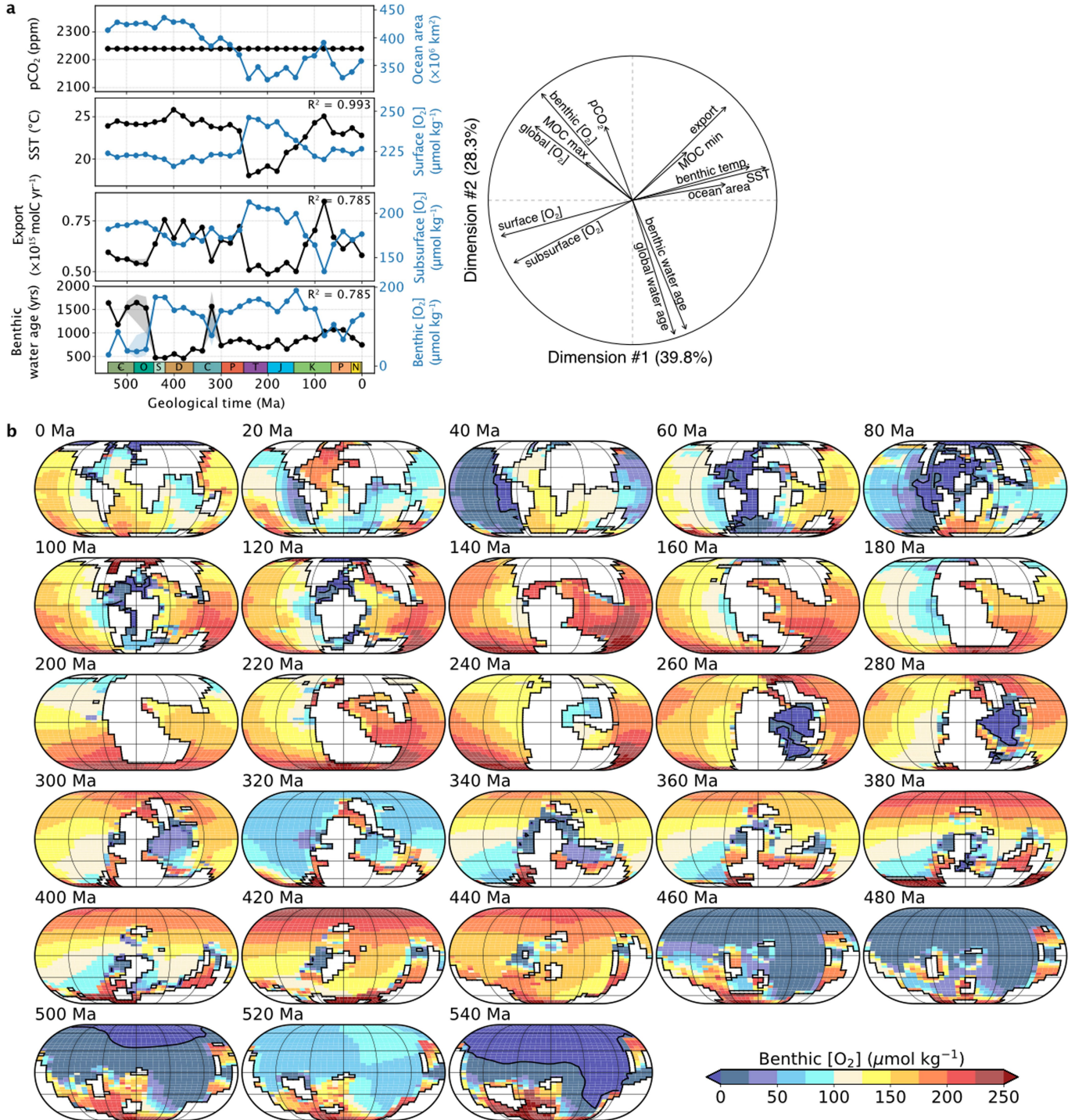


Extended Data Fig. 3 | Deep-ocean circulation for simulations at 2,240 ppm CO₂ (series #1). **a**, Meridional overturning stream function, in Sv (sverdrup, 1 Sv = $10^6 \text{ m}^3 \text{ s}^{-1}$). A negative (blue) stream function corresponds to an anticlockwise circulation. **b**, Annual distribution of convective adjustments across the water column. Emerged continental masses are shaded white. Eckert IV projection. Results are averaged over the last 5,000 years.

Article

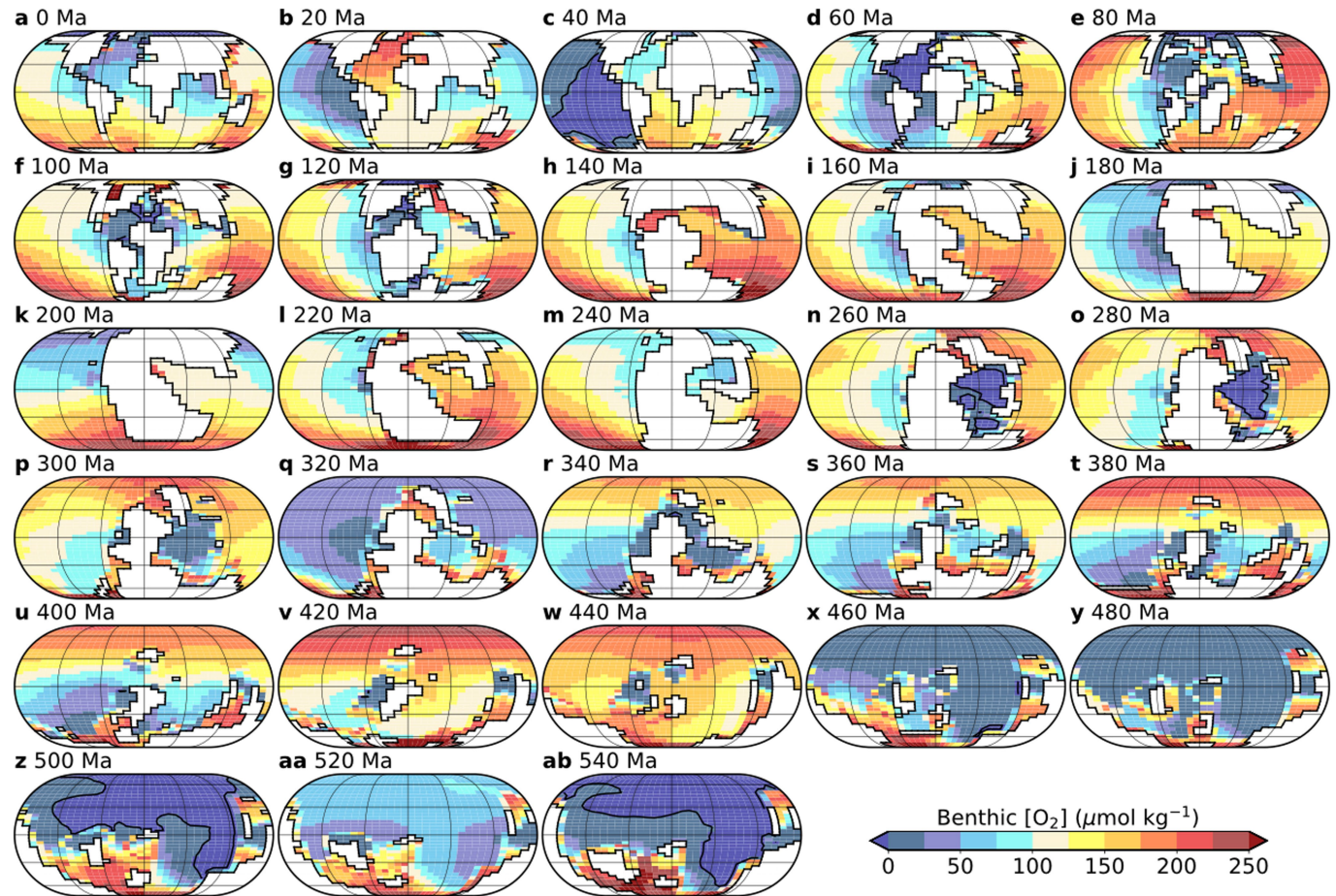


Extended Data Fig. 4 | Sensitivity of benthic $[O_2]$ to the continental reconstruction. Benthic oxygen concentrations for simulations at 2,240 ppm CO_2 (such as series #1) at 440 Ma (a) and 460 Ma (b), using the continental reconstructions of BugPlates³¹, with topography/bathymetry after ref. ⁶¹. Eckert IV projection. Emerged continental masses are shaded white. Results are averaged over the last 5,000 years. Panels a and b are identical to the 440 Ma and 460 Ma panels of Fig. 2, except that simulations have been conducted using another continental reconstruction. Note that, although we simulate sulphate reduction in cGENIE, with SO_4^{2-} being used as the electron acceptor for the remineralization of organic matter in the ocean interior once dissolved O_2 has become depleted (see ref. ⁴⁸), small negative O_2 concentrations can arise when several geochemical reactions compete simultaneously for the same depleted oxygen pool. However, because the product of sulphate reduction—hydrogen sulphide (H_2S)—has fast oxidation kinetics in the presence of free oxygen, the transport of H_2S from anoxic to oxic areas closely mirrors the transport and fate of ‘negative oxygen’ (see ref. ⁶²) and the overall redox landscape is largely independent of this small modelled oxygen overconsumption.



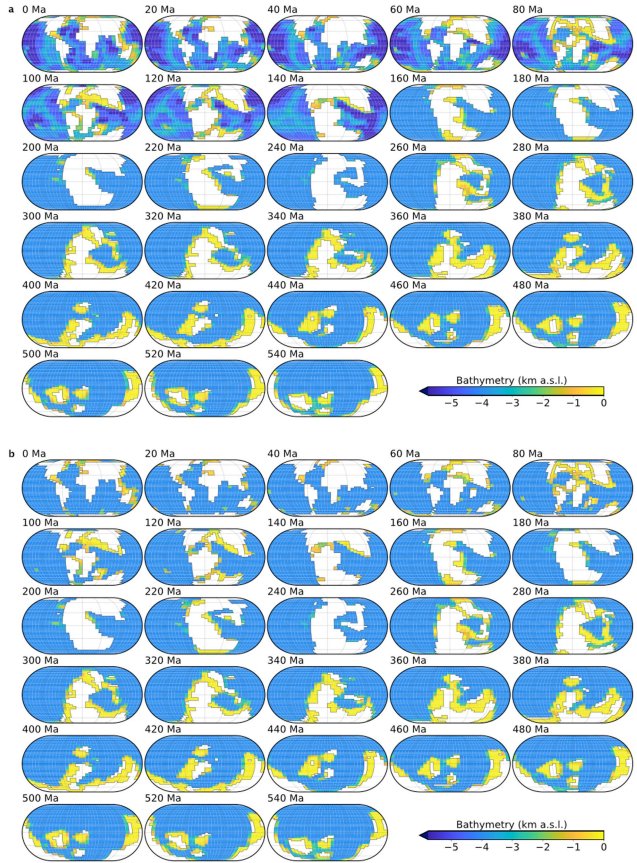
Extended Data Fig. 5 | Sensitivity to the remineralization scheme. Earth system model results for simulations at 2,240 ppm CO₂ (such as #1) but with no dependence of remineralization on temperature. **a**, Same as Fig. 1. **b**, Same as Fig. 2.

Article

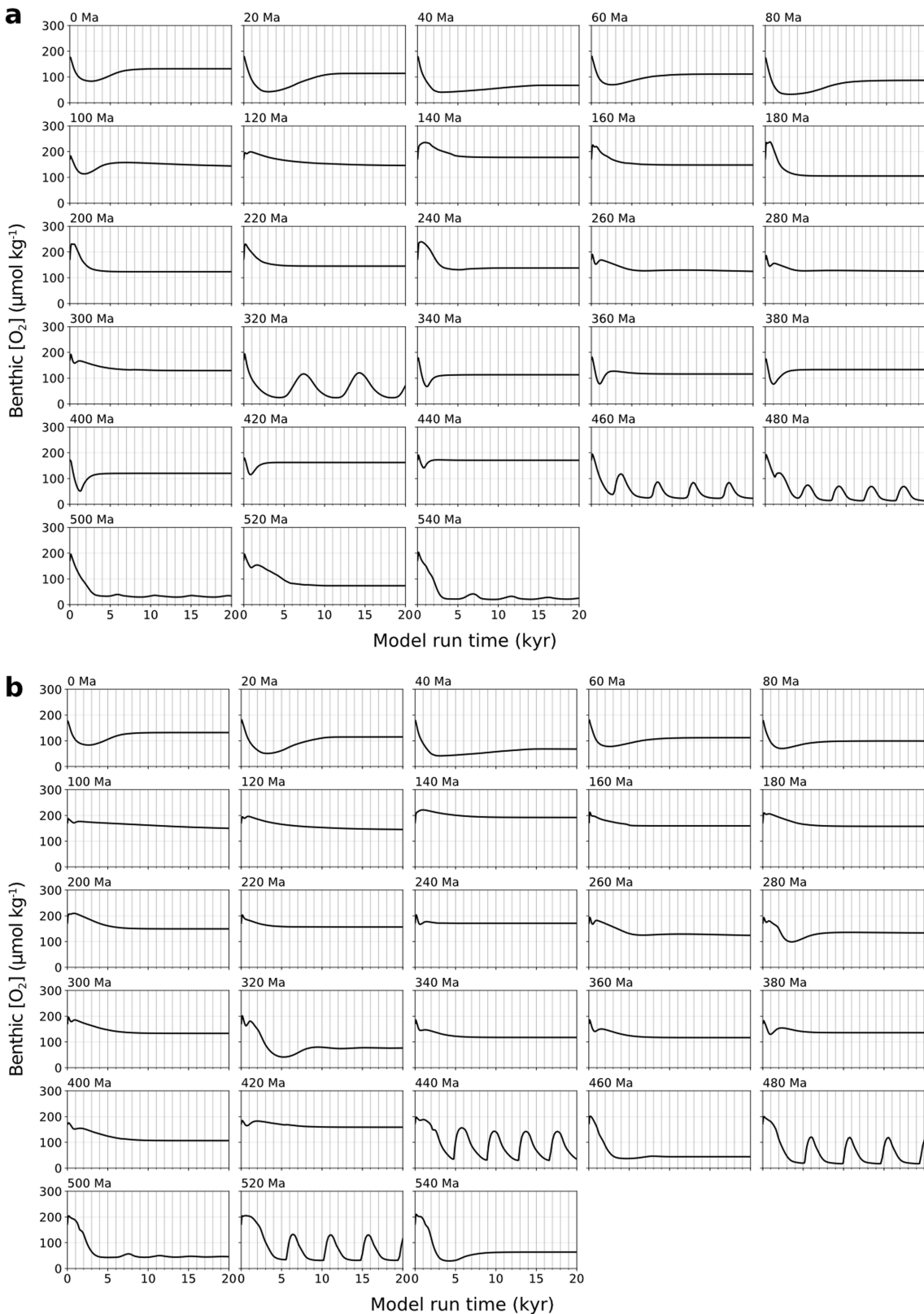


Extended Data Fig. 6 | Sensitivity of benthic $\text{[O}_2]$ to deep-ocean bathymetry. Benthic oxygen concentrations for simulations at 2,240 ppm CO_2 (such as #1) but with no mid-ocean ridges (see Extended Data Fig. 7). Results are

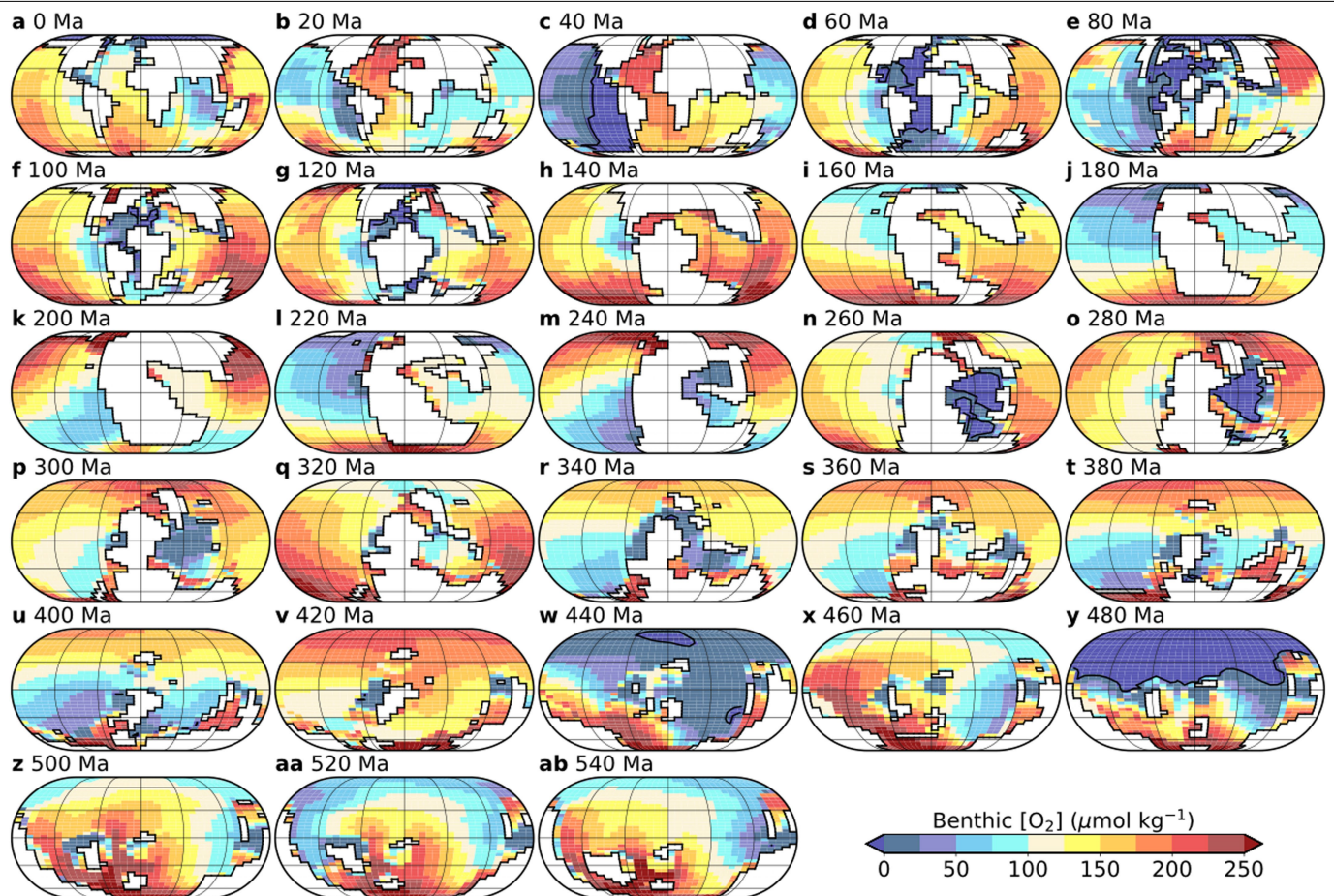
averaged over the last 5,000 years. Emerged continental masses are shaded white. Eckert IV projection.



Extended Data Fig. 7 | Bathymetric reconstructions. Bathymetry with mid-ocean ridges used in series #1 and #2 (**a**) and flat-bottomed bathymetric reconstructions used in simulations with no mid-ocean ridges (**b**) (see Extended Data Fig. 6). Only reconstructions for 0 to 140 Ma (both included) differ (see Methods). Emerged continental masses are shaded white. Eckert IV projection.



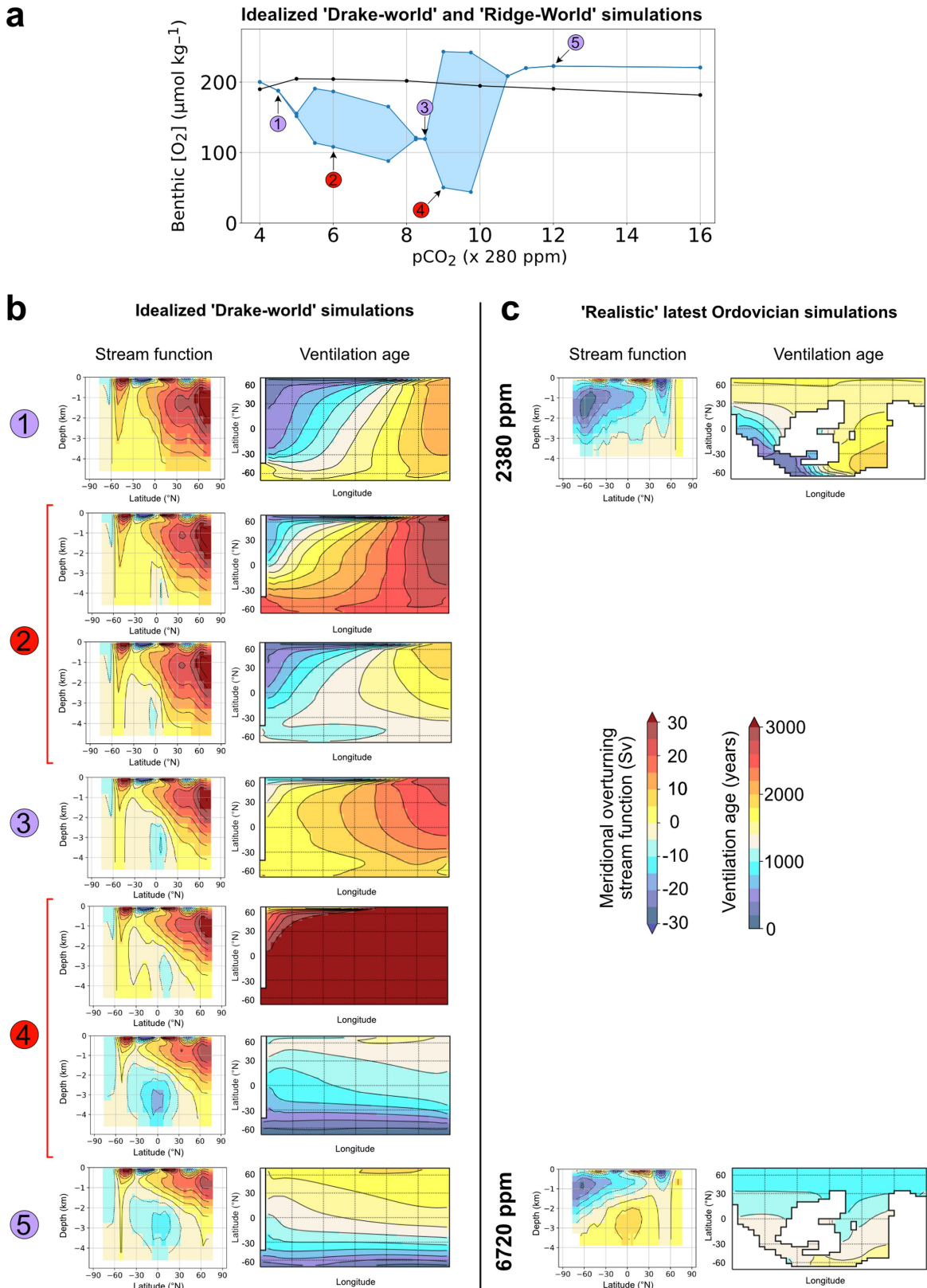
Extended Data Fig. 8 | Time evolution of benthic $[O_2]$. **a**, Simulations at 2,240 ppm CO_2 with temperature-dependent remineralization (series #1). **b**, Simulations in which we varied pCO_2 to approximately ‘correct’ for the palaeogeographical impacts on climate (series #2).



Extended Data Fig. 9 | Sensitivity of benthic $[\text{O}_2]$ to atmospheric forcing ($p\text{CO}_2$). Benthic oxygen concentrations for simulations at 1,120 ppm CO_2 , with temperature-dependent remineralization and mid-ocean ridges. Emerged

continental masses are shaded white. Results are averaged over the last 5,000 years. Eckert IV projection.

Article



Extended Data Fig. 10 | Ocean circulation regimes in the cGENIE model.

a, Envelope of benthic $[O_2]$ values simulated at various atmospheric CO_2 levels using Drake world (in blue, see maps in panel **b**) and ridge world (in black) (Methods). Regimes of stable equilibria and regimes of stable oscillations for Drake world simulations are numbered and labelled using a blue and a red background, respectively. **b**, Meridional overturning stream function in Sv ($1\text{Sv} = 10^6 \text{ m}^3 \text{s}^{-1}$) and map of benthic ventilation age for each stable

equilibrium and the two extreme states of each stable oscillatory regime identified in panel **a**, using the same numbering and colour coding. Lambert cylindrical equal-area projection. A negative (blue) stream function corresponds to an anticlockwise circulation. **c**, Tentative comparison with the latest Ordovician simulations of Pohl et al.²¹. Results are shown at 6,720 ppm and 2,380 ppm CO_2 , corresponding to the warm and cold states of scenario #1 in ref.²¹.